Supplementary Information for
Dynamics of seismogenic volcanic extrusion at Mount St. Helens in 2004-05

R.M. Iverson[1], D. Dzurisin[1], C.A. Gardner[1], T.M. Gerlach[1], R.G. LaHusen[1], M. Lisowski[1], J.J. Major[1], S.D. Malone[2], J.A. Messerich[3], S.C. Moran[1], J.S. Pallister[1], A.I. Qamar[2,4], S.P. Schilling[1], J.W. Vallance[1]

[1]U.S. Geological Survey, Cascades Volcano Observatory, 1300 SE Cardinal Ct. #100, Vancouver, Washington 98683, USA; [2] Earth and Space Sciences, University of Washington, Seattle, Washington 98195, USA; [3] U.S. Geological Survey, Denver Federal Center, Box 25046, Lakewood, Colorado 80225, USA; [4]deceased

List of supplementary information:

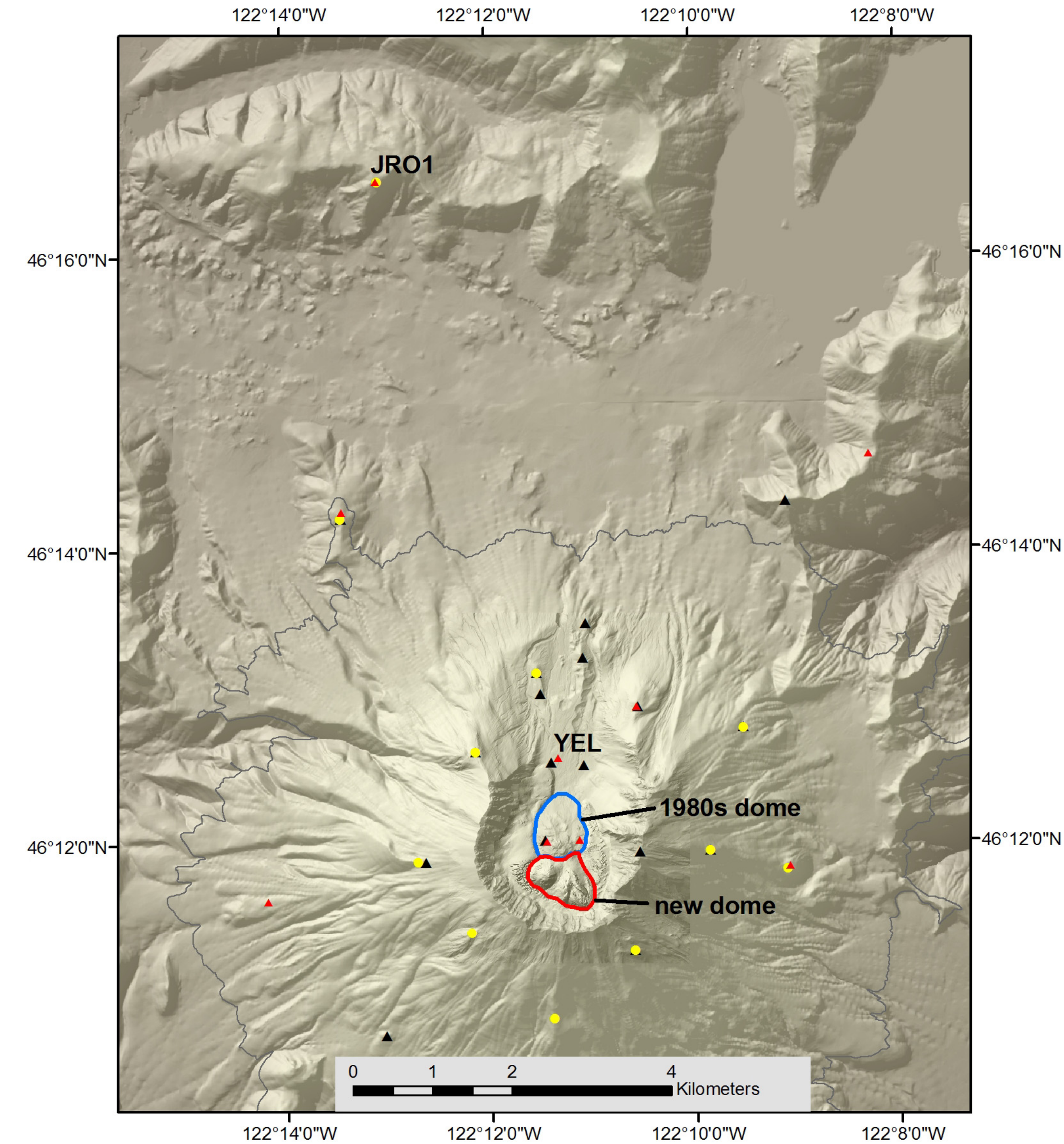

Supplementary Figure 1. Shaded relief map of Mount St. Helens, showing locations of the new (2004-2005) and old (1980-1986) lava domes, seismometers (red triangles) and campaign GPS monuments (black triangles) installed prior to the onset of the 2004-2005 eruption, and of continuous GPS stations installed in October-November, 2004 (yellow circles). An exception is continuous GPS station JRO1, which was installed in May 1997. The irregular gray line surrounding the volcano depicts the 1220 m elevation contour, which roughly defines the base of the modern (< 4000 yrs. b.p.) volcanic edifice.

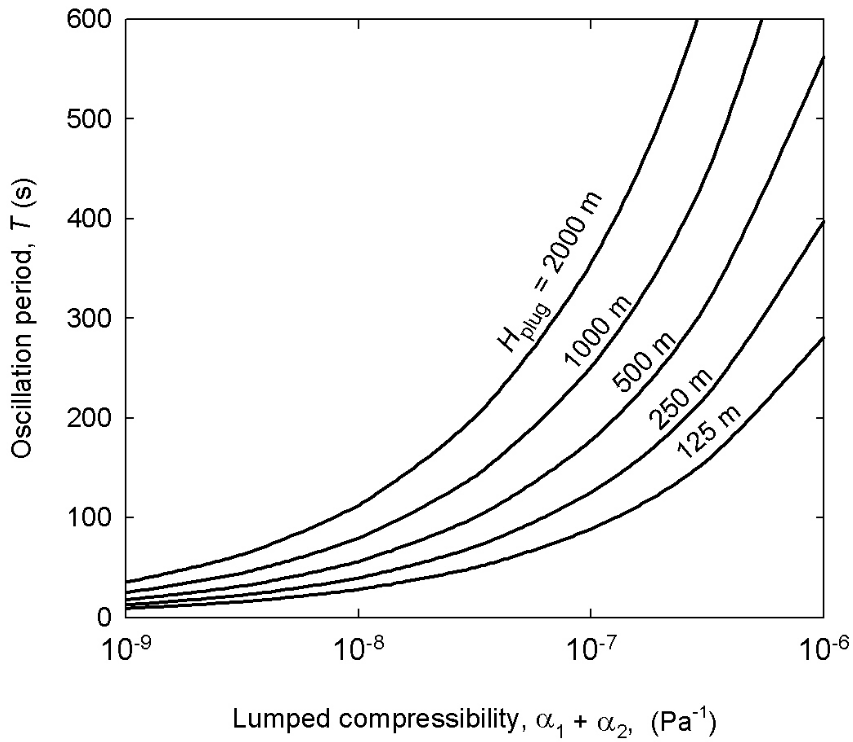

Supplementary Figure 2. Graph of predicted free oscillation period of the plug velocity as a function of the summed magma compressibility α_1 and conduit compliance α_2. Graph applies for the special case in which the plug and conduit are approximated as right cylinders of cross-sectional area A and heights H_{plug} and H_{con}, respectively. In this case the general formula for T reduces to the special form $T = 2\pi[(\alpha_1 + \alpha_2)\rho_r H_{con} H_{plug}]^{1/2}$. The values H_{con} = 8 km and $\rho_r = 2000$ kg/m^3 were used in this formula to generate the graph.

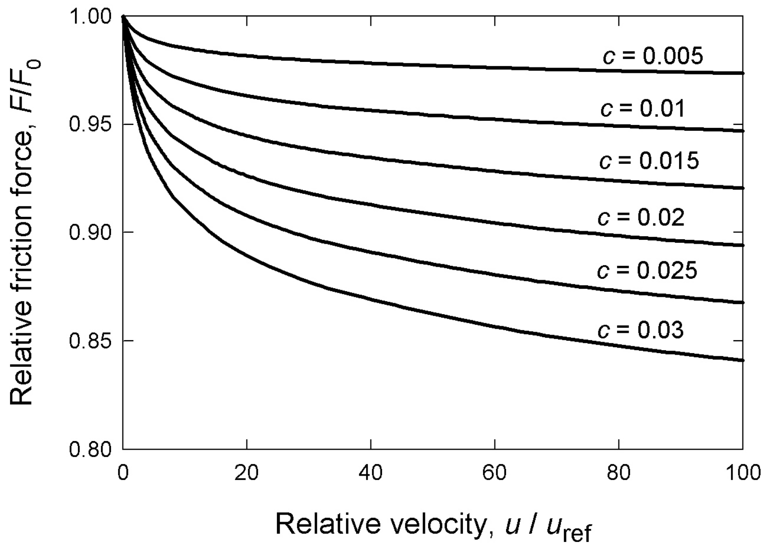

Supplementary Figure 3. Graphs of the friction equation (Eq. 6) for several values of the rate-weakening parameter *c*.

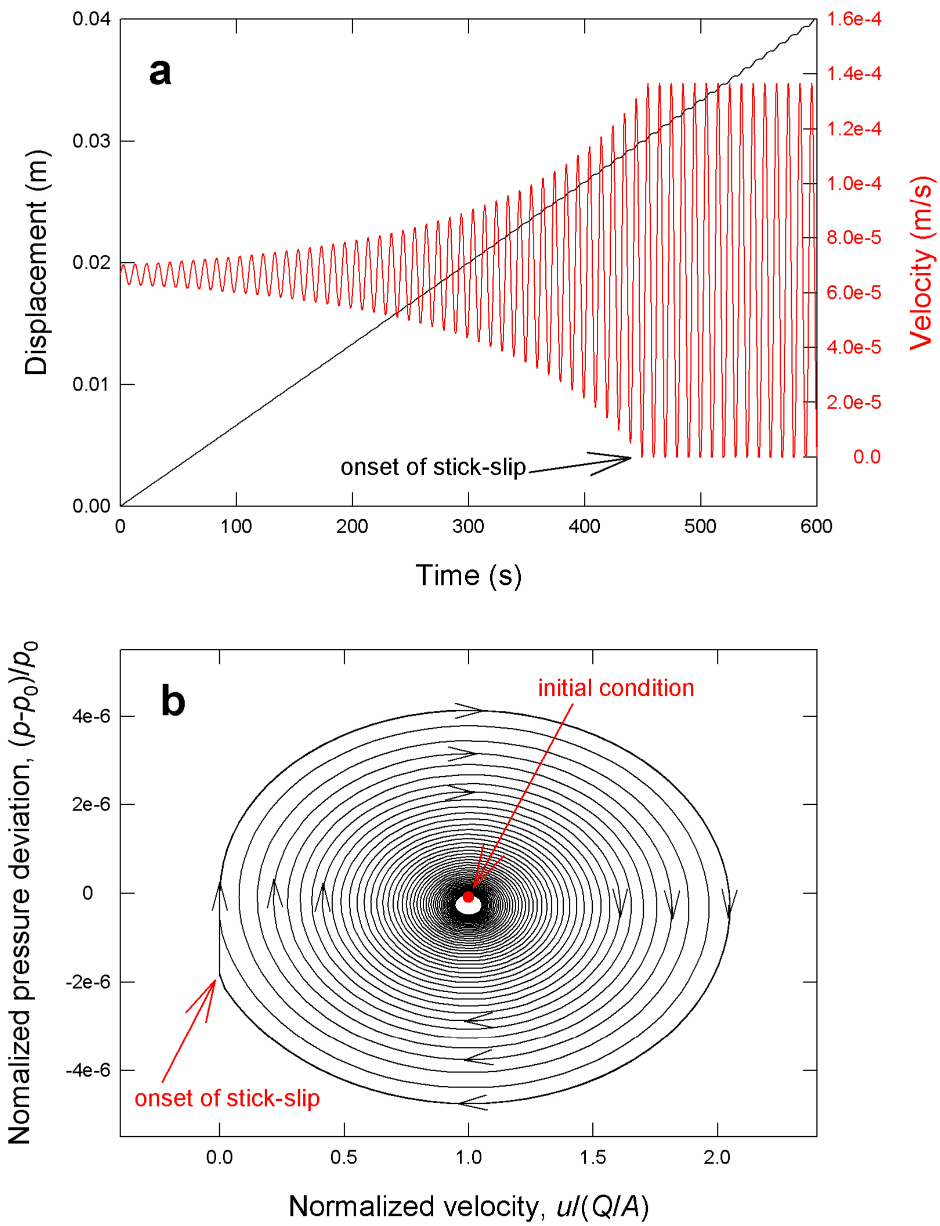

Supplementary Figure 4. Graphs of behavior of the numerical solution of Eqs 1-3 for $D = -0.01$ and an initial condition specifying dynamic equilibrium with $u = Q/A$. The small value of D implies a small value of the limiting equilibrium friction force, F_0. (a) Graph of plug displacement and velocity as functions of time. (b) Phase-plane graph depicting simultaneous evolution of plug velocity and magma pressure. In the phase plane, the dynamics follow the trajectory of a diverging, clockwise spiral until $u = 0$, when repetitive stick-slip limit cycles commence. Arrows point in the direction of advancing time.

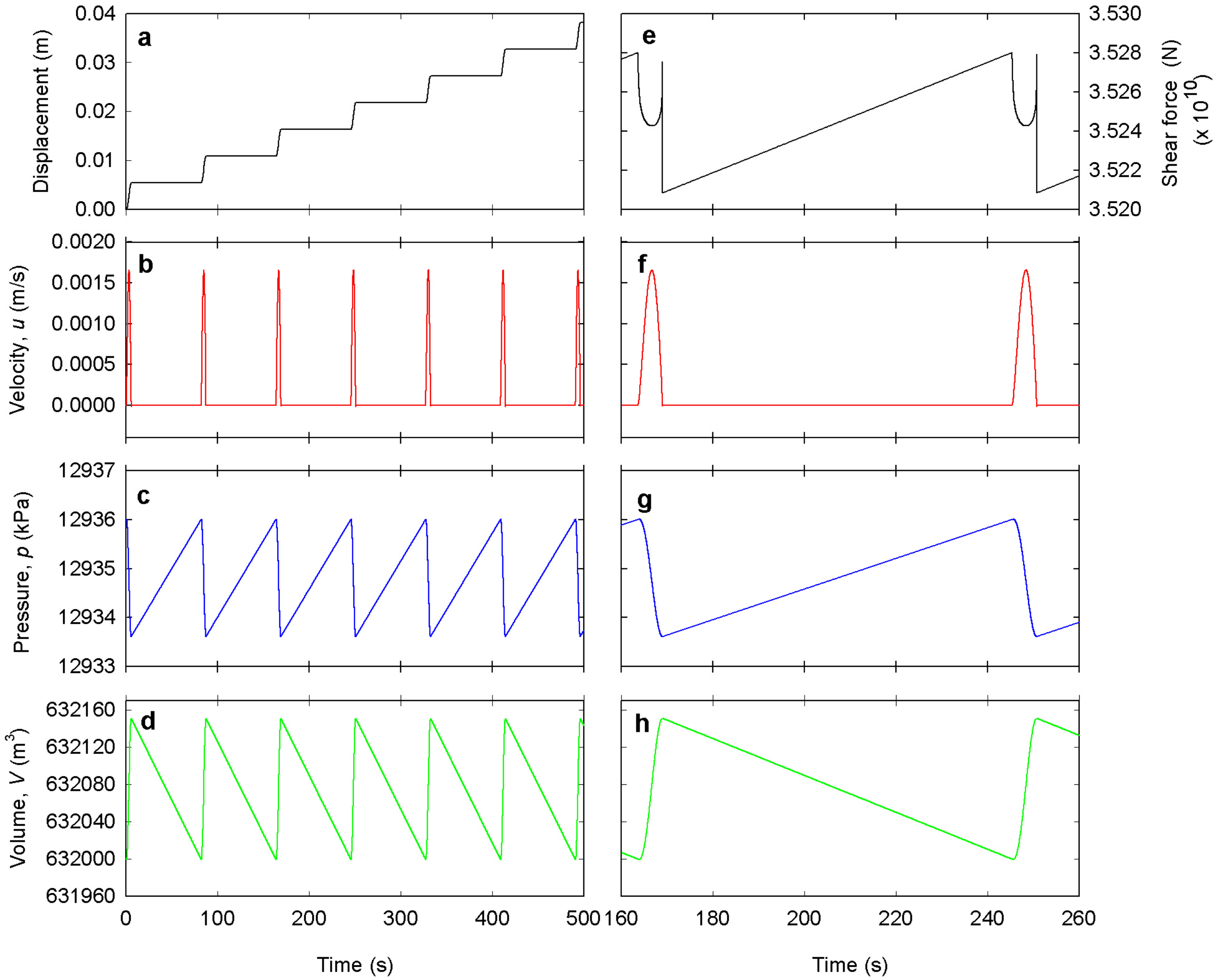

Supplementary Figure 5. Details of stick-slip cycles computed with $D = -2$. This value of D results from use of the parameter values deemed most appropriate for the 2004-2005 eruption of MSH: $A = 30{,}000\ \mathrm{m}^2$, $c = 1.7\times10^{-4}$, $g = 9.8\ \mathrm{m/s}^2$, $m_0 = 3.6\times10^{10}$ kg, $Q = 2$ m^3/s, $u_{ref} = 0.1(Q/A) = 6.67\times10^{-6}$ m/s, $V_0 = 6.3\times10^5\ \mathrm{m}^3$, $\alpha_1 = 1\times10^{-7}\ \mathrm{Pa}^{-1}$, $\alpha_2 = 1\times10^{-9}$ Pa^{-1},and $F_0 = 0.1(m_0 g)$. Panels f, g, and h use an expanded time scale to depict details of two of the seven slip cycles shown in panels a, b, c, and d. Panel e depicts the detailed history of the shear force along the plug margins during the same two slip cycles. Nonlinearly rate-dependent friction results in a complicated force-drop history, including an abrupt drop at the end of each slip cycle.

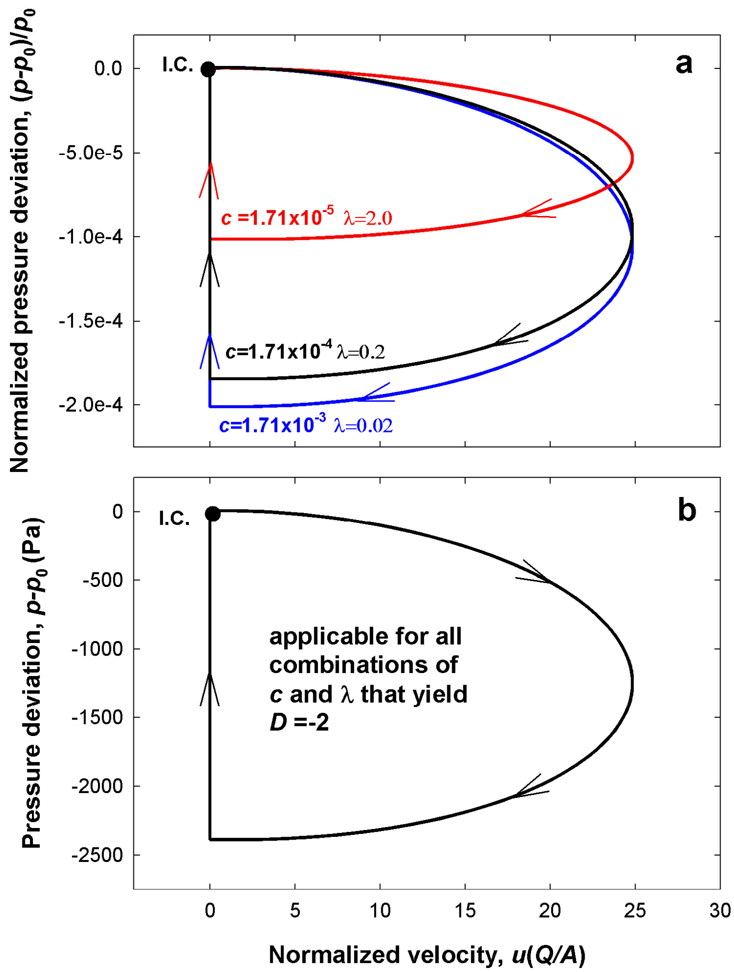

Supplementary Figure 6. Phase-plane representation of limit cycles computed for $D = -2$, with differing combinations of the rate-weakening parameter c and effective-stress parameter λ (which are discussed in detail in the supplementary mathematics section). As shown in (b), pressure deviations from the static equilibrium pressure p_0 do not depend on the values of c and λ individually, although the value of p_0 itself depends on λ, and this variation in λ produces the diverse normalized limit cycles shown in (a).

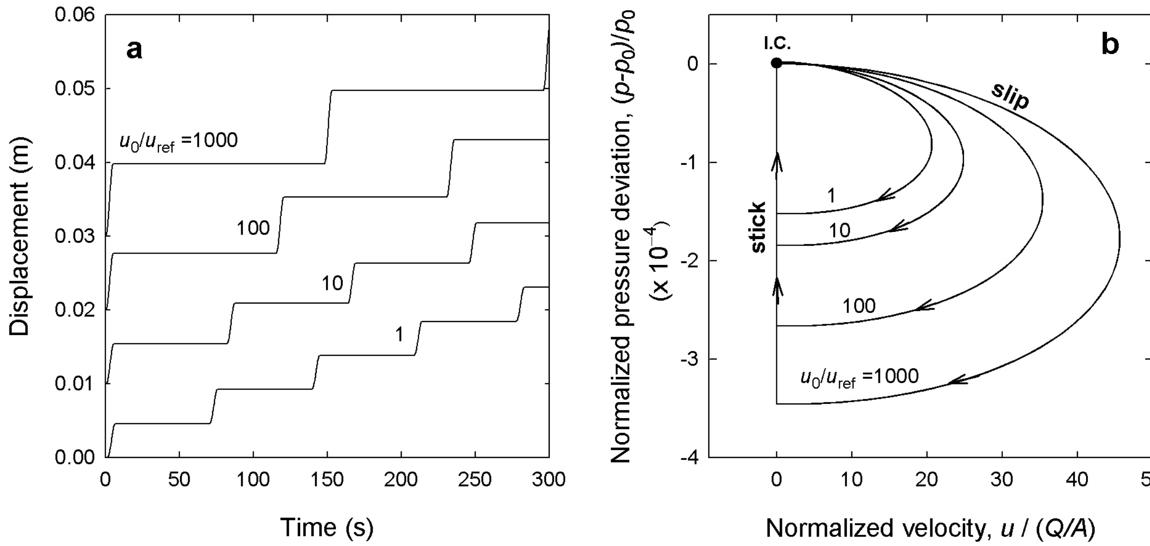

Supplementary Figure 7. Stick-slip extrusion behavior computed for $D = -2$ and various values of the of the velocity ratio u_0 / u_{ref}. Results are depicted as (a) time series, and (b) limit cycles in the velocity-pressure phase plane. Arrows in (b) point in the direction of advancing time. Static equilibrium initial conditions (I.C.) for these calculations were specified by $u = 0$, $p = p_0 = 1.2936\times10^7$ Pa, $V = V_0 = 6.32\times10^5$ m^3, and $\rho = \rho_0 = 2000$ kg/m^3. Note that sensitivity of behavior to variations in u_0 / u_{ref} is much less than the sensitivity to variations in D (compare with Figure 5).

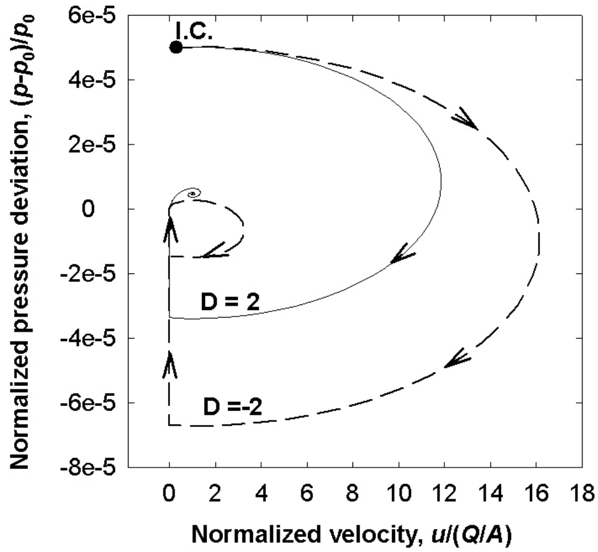

Supplementary Figure 8. Phase-plane diagram computed for a static initial condition (I.C.) with a small disequilibrium pressure, $p / p_0 = 1.00005$. Other initial conditions were the same as those used to generate Figure 5. Results are shown for both rate-strengthening friction ($D = 2$; solid line) and rate-weakening friction ($D = -2$; dashed line). The rate-weakening case converges to the same limit-cycle state shown in Figure 5, whereas the rate-strengthening case converges to a fixed-point equilibrium representing steady-state extrusion.

II. Supplementary Methods

Measurement of Extrusion Rates

Estimates of the changing volume of the newly extruded lava dome were made by differencing digital elevation models (DEMs) compiled from stereoscopic vertical aerial photographs acquired before and during the eruption. Estimates were complicated by the presence of the glacier through which the 2004-2005 lava dome emerged. Beneath the surface of the severely deformed glacier, the distribution of extruded rock is unknown, and this ambiguity produces the biggest source of potential error. For consistency, we report conservative volume estimates made by projecting the perimeter of the visible extrusion vertically downward to the 1986 MSH crater surface, which predates glacier growth.

Volume measurement errors associated with DEM production can be estimated from differences between the locations of photogrammetric control points and locations of the same control points on best-fit mathematical surfaces generated to produce successive DEMs. For DEMs produced from aerial photographs taken about once a month, RMS values of residuals from these fits averaged about 0.17 m in the x and y directions (planimetric coordinates) as well as the z direction (elevation coordinate). Multiplication of 0.17 m by the roughly 1 km^2 area of the MSH crater surface affected by the extrusion yields a volumetric error of 1.7×10^5 m^3, which is about 4% of the typical monthly extruded volume (4×10^6 m^3) inferred from differencing successive DEMs. This error estimate assumes a nearly worst-case scenario, however, as it implies that error occurs systematically rather than randomly.

We estimated apparent linear extrusion rates using monoscopic oblique terrestrial images taken about every three minutes by an automated digital camera positioned along the eastern edge of the mouth of MSH crater, about 2.4 km northeast of the 2004-2005 eruptive vent. We used registered sequential images to track progressive changes in the horizontal and vertical positions of marker points visible on extruding spines. Estimates of actual linear extrusion rate were obtained through trigonometric correction for the difference between the direction of dome extrusion (~155°) and direction of the photographic plane (~117°). In Figure 2, error bars for linear extrusion rates represent ± 1 std. dev. about the mean result obtained by measuring motion of numerous marker points.

Linear extrusion rates inferred from images were calibrated against more precise measurements of linear extrusion rate obtained using GPS. These measurements were accomplished by using helicopter slings to intermittently place expendable GPS instrument packages on extruding spines. Each autonomous package had a single frequency GPS receiver, power, and radio telemetry. GPS positions used to calculate extrusion rate were obtained from single frequency differential solutions for 10 s epochs over baselines extending ~1 km to reference stations. Such solutions are accurate to ~1.5 cm horizontally and ~3 cm vertically. Life spans of instrument packages were typically < 1 week owing to their precarious positioning on extruding, disintegrating spines.

Measurement of Extrusion Temperature

To measure temperatures of extruding spines, airborne thermal imagery was collected every 1 to 4 weeks. The thermal infrared (TIR) camera detected radiation of 8-14 μm wavelengths such that temperatures between -40 and 1500° C were measurable. Measured temperature depended upon emissivity of rock, viewing angle, distance to source, atmospheric temperature, humidity, and steam or clouds if present. These variables were measured independently or minimized such that maximum temperatures reported here are accurate to ±10° C. TIR detected the hottest temperatures of the extruding dome only where cracks and avalanches exposed fresh interior surfaces.

Petrologic, Mineralogic, and Geochemical Methods

We used Fe-Ti oxide equilibration temperatures to compare dacites extruded during the 2004-2005 eruption with dacites extruded at MSH in 1986. The abundance of Fe and Ti in naturally occurring oxide minerals varies with both the temperature and oxygen fugacity. Consequently, where mineral grains of the two solid solutions ilmenite ($FeTiO_3$) - hematite (Fe_2O_3) and magnetite (Fe_3O_4) - ulvöspinel (Fe_2TiO_4) coexist, their compositions can be used to determine the temperature and oxygen fugacity at which the rock or magma was last equilibrated. This relationship was established by experiments by Buddington and Lindsley[28]and is widely applied to determine temperatures and oxygen fugacities of magmas. A temperature of 846 ± 5 °C at an oxygen fugacity of $10^{-12.37\pm0.1}$ was determined for the 2004 dacite using this method and the procedures of Andersen and Lindsay[29] and Stormer[30].

Evidence supporting our inference that magma groundmass crystallization occurred at low pressures includes textural relationships, presence of tridymite or quartz, sodic plagioclase, and anorthoclase as groundmass phases, and the high-silica rhyolite composition of interstitial glass in typical microcrystalline samples of the 2004-2006 dacite. This high silica rhyolite matrix glass plots in the low pressure (0.1-50 MPa) region of the granite minima phase diagram, and the presence of tridymite indicates crystallization at pressures of 10-20 MPa[14]. In addition, a rare glassy fragment of the October 2004 dacite contains 1.87 ± 0.17 wt.% H_20 and <20 ppm CO_2, consistent with the solubility of H_20 in the silicate melt at glass transition pressures of 26-30 MPa[31].

Our measurements of volcanic gas emissions were made by airborne profiling of the emission plume and ambient air by remote (COSPEC, FLYSPEC) and extraction (LI-COR, Interscan) techniques[15]. The cumulative CO_2 released indicates that the 2004-2005 magma was gas-saturated at 8 km depth, despite relatively low gas emission rates (Figure 2). This inference is corroborated by data on the S content of melt inclusions and matrix glasses, which underestimate observed SO_2 emissions by a factor ~ 5.

Earthquake Detection Methods

Because only a fraction of the $>10^6$ earthquakes during the 2004-2005 eruption were manually picked and located, we developed several methods for detecting events automatically and recording event parameters of interest, including the period between earthquakes depicted in Figure 2. The detection method we used to generate this figure employs a standard triggering algorithm that compares average seismic amplitudes computed over short- and long-term time windows. We used averaging windows of 1 second and 8 seconds for the short- and long-term averages, and a triggering ratio of 2.3 that was determined to be optimal for station YEL through trial and error. To avoid multiple triggers from the same event, the detection algorithm skipped forward six seconds after each trigger. We also devised station-specific algorithms for distinguishing between noise glitches (including telemetry and/or internet transmission dropouts, radio interference, and calibration signals) and events, although some glitches still made it through our digital filters. To test the impact of such noise-induced spurious event detections, we visually scanned through seismograms for selected time periods and removed glitches that had been recorded as earthquakes. This process produced cleaner plots but left the basic trends unchanged; in essence, intermittent noise glitches were overwhelmed by the great number of earthquakes.

Geodetic Methods

Together with seismic and volcanic gas techniques, geodetic measurements of ground deformation are an effective tool for monitoring volcanoes and studying volcanic processes. At MSH, both modern instruments and techniques such as the Global Positioning System (GPS), and more traditional ones including photogrammetry and time-lapse photography have been used to study the current eruption. For a discussion of photogrammetric and photographic methods, see *Measurement of Extrusion Rates* above.

Global Positioning System (GPS) observations included surveys in 2000, 2003, and 2004 of a 40-station network of benchmarks concentrated within 10 km of the volcano, but extending more than 30 km in all directions and covering a total area of more than 7400 km^2 (Supplementary Figure 1). Each benchmark was observed for at least two days for each survey. Data were processed using the GIPSY II-OASIS II system[32] developed by the Jet Propulsion Laboratory and installed at USGS Western Region Headquarters in Menlo Park, California. Continuous GPS (CGPS) station JRO1 was established by the USGS Cascades Volcano Observatory (CVO) in May 1997 at the U.S. Forest Service's Johnston Ridge Observatory (Supplemenatry Figure 1). Thirteen additional CGPS stations were installed on or around the volcano in October-November 2004 by CVO and the EarthScope Plate Boundary Observatory (PBO), with two more installed by PBO in February 2005. Data from all 16 CGPS stations are processed at the USGS Menlo Park facility to produce daily 24-hour solutions in a fixed North American reference frame. Scatter in the station position time series is further reduced by regionally filtering the daily solutions[33] using a subset of stable stations located outside the study area to estimate correlated station translations. Results are available at: http://quake.wr.usgs.gov/research/deformation/gps/auto/HelensMonit/.

Elastic load displacements imposed by the growth of the dome are ignored in fitting our model of subsurface deformation to measured surface displacements. Volume change inferred from the model fit is doubled to account conservatively for deformation observed at JRO1 that preceded collection of the 15 October 2004 initial data from the newly installed regional continuous GPS network. The shape and size of the cavity are not well constrained by the deformation data, but the roughly equal amounts of observed horizontal and vertical deformation are consistent with the predictions of deformation resulting from pressure change in a vertically elongate cavity.

III. Supplementary Mathematics

The most fundamental relationships we use to develop our model are equations expressing one-dimensional conservation of mass and linear momentum of the extruding solid plug and underlying fluid magma. These equations are supplemented by three constitutive equations defining magma compressibility, conduit wall-rock compliance, and a friction rule for sliding of the solid plug against the conduit wall. Below we show how the conservation and constitutive equations are combined and reduced to obtain a set of three simultaneous differential equations that describe behavior of the conduit-plug system (Eqs. 1-3 in the main text), and we discuss selection of parameter values used in numerical solutions.

Conservation of linear momentum of solid plug

Changes in the upward momentum of the solid plug are described by Newton's second law of motion, expressed as

$$m \frac{d\,u}{dt} + u \frac{dm}{dt} = p\,A - m\,g - F \tag{S1}$$

where m is the plug mass, u is the upward plug velocity, g is the magnitude of gravitational acceleration, and p is the magma pressure against the base of the plug, which has horizontal area A. Upward motion of the plug is driven by the basal magma pressure force pA and resisted by the weight of the plug mg and a friction force F that results from contact of the plug with the conduit walls.

Conservation of mass of solid plug

Mass change of the solid plug depends on the rate of mass accretion at the base of the plug, $\rho\, B$, and on the rate of mass loss at the surface of plug due to spalling and avalanching, $\rho_r\, E$. Summing these effects yields the mass-conservation equation

$$\frac{d\,m}{dt} = \rho\, B - \rho_r\, E = \kappa \tag{S2}$$

where ρ is the mass density of the magma that congeals to form solid rock at the base of the plug, and B is the volumetric rate of magma conversion to solid rock, which has mass density ρ_r. The parameter E is the volumetric erosion rate of the surface of the plug, and κ is a convenient shorthand for $\rho\, B - \rho_r\, E$. For the sake of simplicity, κ is assumed constant, although this assumption can be relaxed if warranted. With constant κ Eq. S2 yields the explicit solution

$$m = \kappa\, t + m_0 \tag{S3}$$

where m_0 is the initial value of m.

Conservation of linear momentum of conduit fluid

Newton's second law for upward motion of magma in the conduit takes a simple form if variations of magma properties and velocity with position are neglected:

$$\rho \frac{dQ}{dt} + Q\frac{d\rho}{dt} = A\left(\frac{p_b - p}{H} - \rho g - \frac{8\pi\eta}{A^2}Q\right) \tag{S4}$$

Here Q is the vertical (upward) volumetric flux of magma, p_b is the magma pressure at the base of the conduit, and η is the magma viscosity. Eq. S4 is the fluid-mechanical equivalent of Eq. S1 and is also equivalent to the Navier-Stokes equation for one-dimensional laminar flow, integrated over the conduit cross-sectional area A and height H. According to Eq. S4, upward motion of magma in the conduit is driven by the vertical pressure gradient $(p_b - p)/H$ and is resisted by the magma unit weight ρg and viscous drag, represented by the last term in Eq. S4. The form of this drag term is inferred from an elementary analysis of Poiseuille flow in a cylindrical conduit, although other drag terms (e.g., appropriate for other rheologies or conduit geometries) could be used without difficulty.

A simplified momentum equation is obtained by assuming that the magma flux Q is independent of time and making the substitution $dQ/dt = 0$ in Eq. S4. Rearrangement of the resulting equation yields an explicit expression for Q,

$$Q = A\frac{\dfrac{p_b - p}{H} - \rho g}{\dfrac{d\rho}{dt} + \dfrac{8\pi\eta}{A}} \tag{S5}$$

Eq. S5 shows that maintenance of constant Q in the presence of changes in H, p and ρ (which are all possible in the context of this model) can imply compensating changes in p_b. We assume that such compensating changes can occur, but we do not evaluate these changes. A complete evaluation could be accomplished by using Eq. S4 together with a mass-conservation equation (see below) to model the dynamics of transient magma flow in the conduit, but would also require specification of $p_b(t)$ or $Q(t)$ at the base of the conduit. Instead, to streamline our model and focus on the dynamics of the extruding plug, we simply specify a constant basal magma influx Q.

Conservation of mass of conduit fluid

The mass of the fluid magma in the conduit is ρV, where V is the conduit volume. Changes in ρV depend not only on changes in ρ and V but also on the influx of fluid mass at the base of the conduit ρQ and the loss of fluid mass due to plug accretion at the top of the conduit ρB. These phenomena are summarized by the fluid mass-conservation equation

$$\rho \frac{dV}{dt} + V \frac{d\rho}{dt} = \rho(Q - B) \tag{S6}$$

where both Q and B are treated as specified constants.

Constitutive equations

Although the conservation equations for Q and m reduce to the explicit forms shown above, the remaining two conservation equations (S1 and S6) contain four dependent variables, u, p, V, and ρ and an as-yet unspecified friction force F . Therefore, three constitutive equations must be specified to attain mathematical closure.

The first constitutive equation defines the compressibility of the fluid magma α_1 as

$$\alpha_1 = \frac{1}{\rho}\frac{d\rho}{dp} \tag{S7}$$

Combination of this definition with the chain rule $d\rho/dt = (d\rho/dp)\ (dp/dt)$ yields an equation that relates magma density change to pressure change

$$\frac{d\rho}{dt} = \alpha_1 \rho \frac{dp}{dt} \tag{S8}$$

This equation can be used to replace density derivatives with pressure derivatives where advantageous.

A second constitutive equation defines the elastic compliance of the conduit walls α_2 as

$$\alpha_2 = \frac{1}{V}\left[\frac{dV}{dp}\right]_0 \tag{S9}$$

where the subscript 0 denotes conduit volume change under a condition of zero plug velocity ($u = 0$) and zero plug accretion ($B = 0$). The utility of Eq. S9 is increased by embedding the equation in a definition of the total rate of conduit volume change that occurs when u and B are nonzero,

$$\frac{dV}{dt} = A u - \frac{\rho}{\rho_r} B + \left[\frac{dV}{dt}\right]_0 \tag{S10}$$

Here again, the subscript zero denotes the rate of volume change that would exist if $u = 0$ and $B = 0$, whereas the terms Au and $(\rho / \rho_r)B$ describe conduit volume change due to upward plug motion and basal plug accretion, respectively. The factor ρ / ρ_r accounts for the influence of density change from ρ to ρ_r during magma solidification at the volumetric rate B.

To obtain a “systemic” constitutive equation for total conduit volume change, Eq. S9 is embedded in Eq. S10 by using the chain rule $[dV/dp]_0 = [dV/dt]_0 / (dp/dt)$, yielding

$$\frac{dV}{dt} = Au - \frac{\rho}{\rho_r} B + \alpha_2 \frac{dp}{dt} V \tag{S11}$$

The volume change described by Eq. S11 includes both an irreversible component and a reversible (elastic) component.

The third constitutive equation (Eq. 6 of the main text) defines the friction force *F* that appears in Eq. S1. This force is constrained partly by results of laboratory measurements of MSH gouge friction[13], which show that friction exhibits rate-and-state-dependent behavior similar to that observed in tests of other geological materials[26]. Rate dependence of MSH gouge friction is manifested mostly as subtle weakening proportional to the logarithm of slip rate, whereas state dependence is manifested as subtle strengthening proportional to the time the gouge is held in a static state. Although state dependence regularizes the mathematical description of frictional slip of contacting elastic bodies[34], in our model of a sliding rigid body, we consider only rate dependence of friction and omit explicit time dependence. One justification for this omission is that data show that the static strength of MSH gouge increases only a few percent during hold times with durations similar to the ~100 s durations of stick periods inferred for MSH[13]. A second justification is that when slip events occur periodically, as we infer for MSH, variation of strength with hold time has an effect that can be mimicked by upward adjustment of a time-independent static friction coefficient. Finally, and perhaps most importantly, use of a simple rate-dependent friction rule minimizes introduction of constitutive parameters and thereby simplifies our dynamical model. This simplicity greatly facilitates interpretation of analytical and numerical results.

We represent the rate-dependent frictional force *F* with the smooth function

$$F(u/u_{ref}) = F_0\,[1 - c\ \sinh^{-1}(u/u_{ref})] = m_0 g \lambda \mu_0\ [1 - c\ \sinh^{-1}(u/u_{ref})] \tag{S12}$$

where F_0 is a rate-independent static friction force, *c* is a parameter that determines the magnitude of rate dependence, and u_{ref} is a reference plug velocity that determines the nonlinear decay of rate dependence. The force F_0 is defined explicitly as $F_0 = m_0 g \lambda \mu_0$, where $m_0 g$ is the plug weight, μ_0 is a rate-independent static friction coefficient, and the factor λ relates the normal force on the sides of the plug to the plug weight.

Supplementary Figure 3 depicts graphs of Eq. S12 that illustrate how the friction force declines from a static value F_0 as the plug velocity *u* increases. For small plug velocities ($u < u_{ref}$), Eq. S12 indicates that friction exhibits nearly linear rate dependence, $F \approx F_0\ [1 - c\ (u/u_{ref})]$, whereas for large plug velocities ($u > u_{ref}$), Eq. S12 indicates that friction approaches logarithmic rate dependence like that observed in steady sliding experiments with MSH fault gouge[13], $F \approx F_0\,[1 - c\ \ln(2u/u_{ref})]$.

Values of *F* and F_0 depend on values of λ, which in turn depend on the state of effective stress where the plug margins contact the conduit walls. Although this state of stress is not well-constrained at MSH, bounds can nevertheless be placed on applicable values of λ. For example, if $\mu_0 \approx 0.5$ (as shown by experimental data[13]), then the maximum theoretical value of λ is about 2, in which case the plug weight can be supported entirely by static sidewall friction. Applicable values of λ are likely to be considerably smaller than 2, and estimates of λ are constrained by the balance of forces implied by the right-hand side of Eq. S1 for the case of static equilibrium (i.e., $u = 0$): $F = mg\lambda\mu_0 = pA - mg$. Algebraic rearrangement of this balance shows that λ must satisfy $\lambda = (1/\mu_0)[(pA/mg) - 1]$. Therefore, since the magma pressure p is unlikely to deviate much from lithostatic pressure (for if it did, it would cause hydraulic fracturing or conduit collapse) λ is essentially determined by the plug geometry, which determines its mass m and basal area A as well as the depth where p operates. The net effect of these constraints is simple: the value of λ must be consistent with static, limiting equilibrium of the plug when magma pressure is nearly lithostatic.

Reduced governing equations

The equations described above are reduced to a compact system of three equations governing simultaneous evolution of the dependent variables u, V, and p. In this system the magma density ρ is eliminated as an explicit variable by using Eq. S8 to replace $d\rho/dt$ in Eq. S6 with dp/dt and then dividing all terms in the resulting equation by ρ, yielding

$$\frac{dV}{dt} + V\alpha_1 \frac{dp}{dt} = Q - B \tag{S13}$$

Equations S11 and S13 are then combined and rearranged algebraically to obtain explicit equations for dp/dt and dV/dt. These two equations accompany the equation of motion obtained by combining Eqs. S2 and S12 with Eq. S1, thereby forming the set of three simultaneous first-order differential equations:

$$\frac{du}{dt} = -g + \frac{1}{m_0 + \kappa t}\left[pA - \kappa u - F(u/u_{ref}) \right] \tag{S14}$$

$$\frac{dp}{dt} = \frac{-1/V}{\alpha_1 + \alpha_2}\left[Au + RB - Q \right] \tag{S15}$$

$$\frac{dV}{dt} = \frac{\alpha_1}{\alpha_1 + \alpha_2}\left[Au + RB - Q \right] + Q - B \tag{S16}$$

in which R is a variable coefficient defined by

$$R = 1 - \frac{\rho}{\rho_r} = 1 - \frac{\rho_0}{\rho_r}\exp[\alpha_1(p - p_0)] \tag{S17}$$

This expression for R is obtained by solving the isothermal equation of state (S7) that relates the current magma density ρ to the current magma pressure p, and by applying the auxiliary condition $\rho = \rho_0$ when $p = p_0$. Equations S14-S16 are the same as Eqs 1-3 in the main text.

Parameter values used in numerical solutions

As described in the main text, the solutions we present of equations S14-S17 assume B = Q, $\kappa = 0$ and $u_{ref} = 0.1(Q/A)$, but these values can be changed within reasonable bounds with only slight effects on results. The chief effect of $B \neq Q$ is to cause the magma-column volume V to grow or decline subtly with time, with consequent subtle effects on periods and amplitudes of oscillations. Use of $\kappa \neq 0$ also modifies oscillation periods and amplitudes, and additionally it modifies the effective damping D, as indicated by Eq. 5 of the main text. However, these modifications are subtle provided that $\kappa \Delta t / m << 1$ for any time interval Δt. Cases in which this criterion would be violated include those in which the mass of the extruding plug changes suddenly as a consequence of a large gravitational collapse. In such cases a sudden shift in oscillation period and amplitude would be expected. If u_{ref} is smaller than the value $u_{ref} = u_0 = Q/A$, the effect on results is subtle, as any value this small ensures that rate-dependent friction is predominantly in the range of logarithmic decay (see Supplementary Figures 3 and 7). On the other hand, use of large u_{ref} values (larger than $\sim Q/A$) causes frictional rate weakening to be more pronounced (i.e., more nearly linear) at low slip rates, and it consequently increases the tendency toward instability, as manifested by larger, more abrupt slip events. This effect is inherently nonlinear, but much of the effect of u_{ref} is nevertheless absorbed by changes in the damping parameter D, as described below.

With adoption of fixed values of B, κ, and u_{ref}, as noted above, a complete suite of model results can be presented concisely because results depend entirely on initial conditions and values of the natural timescale t_0 and dimensionless damping parameter D evaluated at the equilibrium slip rate $u = u_0 = Q/A$. These D values represent the combined effects of all the constitutive and geometric parameters in the model. The expression for D at $u = u_0$ is derived as described in the main text (Figure 5 caption), yielding the result:

$$D = \frac{-t_0\, g\, c\, \lambda\, \mu_0}{2u_{ref}\left[1 + \left(\dfrac{u_0}{u_{ref}}\right)^2\right]^{1/2}} \tag{S18}$$

where $t_0 = \left[m_0(\alpha_1 + \alpha_2)V_0\right]^{1/2} / A$. The numerator of right-hand side of Eq. S18 can alternatively be expressed as $-F_0 t_0 c / m_0$; thus, the magnitude of the static friction force F_0 is implicit in the value of D, provided that values of the other parameters in Eq. S18 are known. If $u_0 / u_{ref} >> 1$, as will be true if typical slip rates are in the logarthimic weakening regime, then the denominator on the right-hand side of Eq. S18 can be approximated as $2u_0$. Thus, an approximate version of Eq. S18 that is applicable in most circumstances of interest is $D \approx -t_0 gc\lambda\mu_0 / 2u_0$.

In our model calculations, the combination of parameter values we used to obtain $D = -2$ (our estimate of the appropriate D value for the 2004-2005 eruption of Mount St. Helens) is: $A = 30{,}000$ m^2, $c = 1.7\times10^{-4}$, $g = 9.8$ m/s^2, $m_0 = 3.6\times10^{10}$ kg, $Q = 2$ m^3/s, $u_{ref} = 0.1(Q/A) = 6.67\times10^{-6}$ m/s, $V_0 = 6.3\times10^5$ m^3, $\alpha_1 = 1\times10^{-7}$ Pa^{-1}, $\alpha_2 = 1\times10^{-9}$ Pa^{-1}, $\lambda = 0.2$, and $\mu_0 = 0.5$. Although these values represent reasonable estimates, alternative combinations of values that yield $D = -2$ produce results that differ only subtly, provided that the natural timescale t_0 is unchanged and $(Q/A)/u_{ref} >> 1$ (Supplementary Figures 6 and 7).

IV. Supplementary Notes

28. Buddington, A.F., & Lindsley, D.H. Iron-titanium oxide minerals and synthetic equivalents. *Journal of Petrology* **54**, 310-357 (1964).

29. Andersen, D.H., & Lindsay, J.R. Internally consistent solution models for Fe-Mg-Mn-Ti oxides. *American Mineralogist* **73**, 714-726 (1988).

30. Stormer, J.C. The effects of recalculation on estimates of temperature and oxygen fugacity from analyses of multi-component iron-titanium oxides. *American Mineralogist* **68**, 586-594 (1983).

31. Moore, G., Vennemann, T., & Carmichael, I.S.E. Solubility of water in magma to 2 kbar: *Geology* **23**, 1099-1102 (1995).

32. Zumberge, J.F., Heflin, M.B., Jefferson, D.C., Watkins, M.M., & Webb, F.H. Precise point positioning for the efficient and robust analysis of GPS data from large networks. *J. Geophys. Res*. **102** (B3), 5005-5017 (1997).

33. Wdowinski, S., Bock, Y., Zhang, J., Fang, P., & Genrich, J. Southern California permanent GPS geodetic array: Spatial filtering of daily positions for estimating coseismic and postseismic displacements induced by the 1992 Landers earthquake, *J. Geophys. Res*. **102** (B8), 18,057-18,070 (1997).

34. Rice, J.R., Lapusta, N., & Ranjith, K. Rate and state dependent friction and the stability of sliding between elastically deformable solids. *Journal of the Mechanics and Physics of Solids* **49**, 1865-1898 (2001).

V. Legends for Supplementary Movies 1 and 2

MSH DEM sequence.mpg: This movie shows a sequence of vertical shaded relief images illustrating dome growth and accompanying glacier deformation at Mount St. Helens, 2004-2005. Images were produced from digital elevation models (DEMs) constructed from stereoscopic aerial photographs taken roughly once a month.

MSH timelapse photo sequence.mpg: This movie shows a sequence of terrestrial photographs illustrating dome growth at Mount St. Helens, 2004-2005. The movie was compiled from photographs taken about once every three minutes by an automated digital camera. Gaps in the photo sequence occur where clouds or heavy precipitation obscured the view of the dome. View is from a site known as Sugarbowl, located 2.3 km northeast of the 2004-2005 vent.